ORIGINAL PAPER

Improving Coking Resistance and Catalytic Performance of Ni Catalyst from LaNiO$_3$ Perovskite by Dispersion on SBA-15 Mesoporous Silica for Hydrogen Production by Steam Reforming of Ethanol

Isa Carolina Silva Costa[1] · Elisabete Moreira Assaf[2] · José Mansur Assaf[1] (ORCID)

Abstract

A strategic option for the production of H$_2$ from renewable resources is use of the ethanol steam reforming reaction. Catalysts based on nickel have been widely investigated for this reaction, offering the advantages of low cost and high activity. However, a difficulty is that nickel may be strongly deactivated by coke formation. Perovskite-type mixed oxides are promising precursors for nickel-based catalysts, since their reduction leads to the formation of highly dispersed metal particles that can mitigate carbon deposition. However, high calcination temperatures are required for perovskite structure formation, resulting in low surface areas and limiting the effectiveness of this method. In order to address this difficulty, the present work proposes a novel strategy whereby the perovskite-type oxide LaNiO$_3$ is supported on SBA-15. Characterization of the catalysts was performed using XRF, XRD, SEM, TPR, TEM, BET, H$_2$-TPD, and TGA techniques. Their performances were then evaluated in catalysis of the ethanol steam reforming reaction to produce hydrogen. Calcination at 750 °C resulted in formation of highly dispersed perovskite on a support that presented high specific surface area. The catalyst obtained from reduced LaNiO$_3$/SBA-15 with 33 wt% perovskite was the most active in the reaction. Analyses using TGA and SEM showed the formation of carbon mainly over Ni catalysts obtained from bulk LaNiO$_3$ perovskite, while supporting LaNiO$_3$ on SBA-15 led to lower deposition of carbon. The superior performance of this material in catalysis could be attributed to the dispersion of the perovskite on SBA-15, resulting in smaller size of the Ni metal particles formed during the reduction, compared to the catalyst derived from bulk perovskite. This promising method could be used in the production of a wide range of other catalysts.

Keywords Perovskite · SBA-15 · Ni · Steam reforming · Ethanol · Carbon deposition

1 Introduction

There is an urgent need to reduce dependence on traditional sources of energy including oil, coal, and natural gas, in order to minimize environmental impacts and ensure energy security. Consequently, with the increase of energy consumption and the depletion of fossil feedstocks, there is increasing interest in the development of alternative renewable energy resources [1, 2].

Hydrogen is especially important as an alternative source of energy, because the only byproduct formed during its combustion is water, and its energy content per mass is high, compared to petroleum. This high efficiency, when combined with fuel cells for energy generation, provides a highly promising technology [3–5]. Currently, most of the hydrogen produced comes from steam reforming of methane, which is the main component of natural gas, a fossil fuel. From an operational point of view, this process is still the most economical and viable method for the generation of hydrogen. Nonetheless, studies have investigated the production of hydrogen from renewable sources, such as liquid biofuels derived from biomass, which are environmentally more attractive [6, 7]. In Brazil, there is high potential for applying these renewable sources to obtain hydrogen, since

✉ José Mansur Assaf
mansur@ufscar.br

1 Laboratório de Catálise, Departamento de Engenharia Química, Universidade Federal de São Carlos, Rod. Washington Luis, km 235, São Carlos, São Paulo, Brazil

2 Instituto de Química de São Carlos, Universidade de São Paulo, Av. Trabalhador São-Carlense, 400, São Carlos, São Paulo, Brazil

the country has one of the most successful programs for the production of bioethanol from sugarcane fermentation. It is evident that the production of H_2 from renewable resources such as ethanol can provide clear environmental benefits [8–10].

The ethanol steam reforming reaction is an excellent strategy for production of H_2. Nonetheless, although significant efforts have been made, there is a need for further work to develop catalysts providing high performance [8, 10]. Catalysts based on nickel offer the greatest promise for industrial ethanol steam reforming, because they are inexpensive and present high activity, when compared with noble metals [11]. However, a difficulty is that they can undergo strong deactivation, due to the deposition of carbon [12, 13]. A method that can be used to minimize carbon deposition is to control the nickel particle size by using perovskite-type oxides as catalyst precursors [14–16]. The reduction of this type of mixed oxide results in the formation of small metal particles that are highly dispersed [17, 18] and on which carbon formation is hindered [19, 20]. Unfortunately, high calcination temperatures are required for formation of the perovskite structure, resulting in low surface areas (generally below 10 m^2 g^{-1}) and limiting the effectiveness of this strategy [17, 21].

A promising way to avoid these difficulties is to obtain perovskite highly dispersed on a support with high specific surface area [11, 21]. The literature reports various supported perovskite-type oxides used in different reactions [22–24]. Wang et al. (2013) evaluated the performances of nickel-based catalysts obtained from bulk $LaNiO_3$ perovskite, as well as $LaNiO_3$ perovskite supported on several mesoporous silicas (SBA-15, MCM-41, and SiO_2), which were used in the dry reforming of methane. The supported catalysts presented much improved activity and stability, compared to the bulk perovskite. The supported catalyst that showed the highest stability was $LaNiO_3$/SBA-15, which was attributed to the good thermal stability of SBA-15 [24]. Marinho et al. (2016) studied ethanol steam reforming using Ni-based catalysts produced from the perovskite-type oxides $LaNiO_3$ and $LaNiO_3$/$CeSiO_2$. Lower carbon formation was observed for the $LaNiO_3$ supported on $CeSiO_2$, which could be explained by the degree of dispersion of Ni, as well as the provision of oxygen to the metal surface, promoted by the support. Supported perovskite catalysts usually offer advantages, compared to unsupported catalysts, but there have been few published studies concerning the performance of catalysts obtained from supported perovskites, when used in the ethanol steam reforming reaction [25].

Therefore, the objective of the present study was to investigate the performance of nickel-based catalysts produced using bulk $LaNiO_3$ perovskite or $LaNiO_3$ perovskite supported on SBA-15 mesoporous silica, for hydrogen production employing the ethanol steam reforming reaction. The

physical–chemical properties of the catalysts were elucidated using different characterization techniques. Evaluation was then made of the relationship between catalytic performance and the properties of the materials.

2 Experimental

2.1 Catalyst Preparation

Bulk $LaNiO_3$ perovskite was obtained by the citrate complexing method, also known as the modified Pechini method, as described by Liu et al. (2015) and Toniolo (2010), with modifications [16, 26]. Briefly, stoichiometric amounts of nickel and lanthanum nitrates (1.221 and 1.781 g, respectively) were solubilized in deionized water (10 mL), followed by addition of citric acid (1.887 g) to give a total metal cation/citric acid molar ratio of 1:1.2. This mixed solution was stirred for 30 min, at 60 °C, before addition of ethylene glycol (0.405 g) to give a citric acid/ethylene glycol molar ratio of 3:2. The solution obtained was then concentrated by heating at 90 °C, until a spongy solid was formed. This solid was dried for 12 h at 100 °C, followed by calcination, under a flow of air, at 170, 500, and 750 °C for 2, 4, and 5 h, respectively, employing a heating rate of 2 °C min^{-1}. The catalyst derived from $LaNiO_3$ was denoted LN.

SBA-15 was synthesized according to a hydrothermal method based on the procedure developed by Zhao et al. [27, 28] and Oemar et al. [29]. Firstly, the Pluronic 123 (P123) triblock copolymer surfactant (2.828 g) was added to deionized water (75 mL), followed by addition of 37 wt% hydrochloric acid (HCl) (14 mL). The mixture was maintained under stirring for 2 h, at 35 °C, before addition of tetraethyl orthosilicate (TEOS) (6.122 g) and maintaining under agitation for 24 h at 35 °C. The resultant gel was placed in a polypropylene bottle and hydrothermal treatment in an oven for 48 h, at 90 °C, under static conditions. The silica obtained was filtered, washed with copious amounts of deionized water until reaching pH 7, and dried overnight at 60 °C in an oven. Subsequently, calcination was performed for 3 h, at 550 °C, using a heating rate of 1 °C min^{-1}. The reagents molar ratio was fixed at 1 TEOS: 0.0169 P123: 5.85 HCl: 142 deionized water.

The loading of $LaNiO_3$ on the SBA-15 support was performed using a procedure combining incipient wetness impregnation with citrate complexing, as described by Zhao et al. [30] and Li et al. [31], with modifications. This method of preparation of the supported $LaNiO_3$ perovskite was similar to the synthesis of the bulk perovskite, described above. Firstly, the nickel and lanthanum nitrates (0.305 g and 0.445 g, respectively) were solubilized in deionized water (5 mL), together with citric acid (0.472 g). The resulting solution was stirred for 30 min, at 60 °C, in order to ensure

complexation of all the ions. Ethylene glycol (0.101 g) was then added to the mixed nitrate solution, under stirring. The total metal cation/citric acid and citric acid/ethylene glycol molar ratios were kept at 1/1.2 and 3/2, respectively. The aqueous solution obtained was stirred for 30 min, at 60 °C, prior to addition of the SBA-15 support. The support dispersed in deionized water was then added slowly into the solution. In a typical synthesis, 0.5 g of SBA-15 was dispersed in 5 mL of deionized water, with stirring for 4 h at room temperature, followed by evaporation of the solvent under vacuum, using a rotary evaporator. This was a crucial step to ensure that the aqueous solution impregnated the mesopores of the support. After drying, the material was calcined under the same conditions used for the bulk perovskite, described above. The LaNiO$_3$ supported on SBA-15 was denoted 33LN/SBA-15, with 33 wt% of perovskite in the material. The content of perovskite used in the supported catalysts (33%) was based in a previous study performed by our group, which evaluated the ethanol conversion and hydrogen yield.

2.2 Characterization of the Catalysts

The catalyst crystalline structures were investigated by X-ray diffraction (XRD), using a Rigaku Miniflex diffractometer, with Cu Kα radiation ($\lambda = 0.15496$ nm). The diffractograms were collected in a wide angle between 10° and 80° (2θ) (step = 0.02 and speed = 10°/min), for the bulk and supported perovskite, and at low angles between 1° and 5° (2θ) (step = 0.02 and speed = 10°/min), for SBA-15 and the supported perovskite. The metallic Ni crystallite size was calculated from the X-ray patterns using the Scherrer equation.

The catalyst surface areas were determined by the BET method, using a partial pressure range of 0–0.3. The pore size distributions and pore volumes were obtained from the desorption isotherm, according to the BJH (Barret–Joyner–Halenda) method. The assays employed a Micrometrics ASAP 2020 instrument, with N$_2$ adsorption at − 196 °C. Before starting the N$_2$ adsorption, the sample (100 mg) was degassed under vacuum for 2 h, at 200 °C, for removal of physisorbed substances.

The chemical compositions of the samples were analyzed by X-ray fluorescence spectrometry, using an energy dispersive X-ray spectrometer (Ray Ny EDX-720, Shimadzu), with emission of gamma radiation from the element rhodium.

Temperature-programmed reduction (TPR) analyses were performed by chemisorption, using a Micromeritics AutoChem II instrument. A sample mass of 75 mg (60–100 mesh) was heated from ambient temperature to 800 °C, at a rate of 10 °C min^{-1}, under a 20 mL min^{-1} flow of 10% H$_2$ in N$_2$. The consumption of H$_2$ was measured using a thermal conductivity detector (TCD). Before the measurements, the samples were pretreated for 1 h at 200 °C, under a flow of

N$_2$, in order to remove adsorbed H$_2$O, followed by cooling to ambient temperature (under N$_2$).

The metallic area was determined by temperature-programmed hydrogen desorption (H$_2$-TPD), using an Auto-Chem II instrument. The sample (0.150 g) was reduced for 1 h, at 750 °C, under a flow of H$_2$. After cooling to 50 °C, purging was performed for 30 min, under a flow of N$_2$. Chemisorption of H$_2$ was performed at 50 °C, under a flow of H$_2$, followed by purging for 16 h, under a flow of N$_2$, to remove physisorbed H$_2$. In the H$_2$-TPD step, the sample was heated from 50 to 600 °C, at 10 °C min^{-1}, under a flow of N$_2$. The amount of hydrogen desorbed was determined using a TCD detector.

Transmission electron microscopy (TEM) images were acquired using an FEI TECNAI G^2 F20 instrument operating at 200 kV. For the analyses, the powder samples were dispersed in isopropanol, under ultrasonication, and deposited onto copper grids coated with a film of holey carbon. Scanning electron microscopy (SEM) images were acquired using an FEI Magellan 400 L instrument.

Thermogravimetric analyses (TGA) were performed using a simultaneous DTA-TGA analyzer (ATG-DTG 60 H, Shimadzu), in order to determine the amounts of coke present on the exhausted catalysts. For this, the exhausted catalyst (~ 10 mg) was heated from ambient temperature to 1000 °C, at 10 °C min^{-1}, under a flow of air. The weight change was calculated as follows:

$$\frac{W_1 - W_2}{W_1} * 100\% \tag{1}$$

where, W_1 and W_2 are the initial and final weights of the exhausted catalyst, respectively.

2.3 Catalytic Activity Measurement

The assays of catalytic activity in the ethanol steam reforming reaction were performed at atmospheric pressure, using a continuous flow fixed-bed reactor. The catalyst (60–100 mesh grain size) was placed between layers of quartz wool, in a tubular reactor. In order to ensure that the amounts of nickel were the same in the assays using the catalyst derived from bulk material and the catalyst with perovskite supported at 33 wt% on SBA-15, amounts of 33 and 100 mg of LN and 33LN/SBA-15 were used, respectively. Before the reaction, the catalyst precursor was reduced for 1 h, at 750 °C, under a flow of pure H$_2$ (30 mL min^{-1}), in order to generate the active sites for the reaction. The system was then cooled to the reaction temperature during 30 min, under a flow of N$_2$. A pump was used to stoichiometrically feed the liquid mixture of reactants (H$_2$O/ethanol molar ratio of 3.0) into the reactor, at a flow rate of 1.7 mL h^{-1}, with vaporization at 180 °C. The catalytic reaction assays were performed

during 5 h, at 550 °C. The activity and stability of the catalysts were evaluated by performing the ethanol steam reforming reaction with and without the use of carrier gas (N_2, at 100 mL min^{-1}). The gaseous products at the outlet were analyzed online using a gas chromatograph (CG-3800, Varian) equipped with two columns in parallel (Porapak N and Molecular Sieve 13X), each connected to a TCD. After the reactions, the condensed liquid products were recovered for analysis using a Shimadzu gas chromatograph equipped with an RTX1 capillary column and an FID detector. The ethanol conversion ($X_{Ethanol}$, %), hydrogen yield ($Y_{Hydrogen}$), and mean product selectivity (S_i, %) or selectivity of products versus time on stream (S_i, *mol of product/mol of ethanol converted*) were determined using Eqs. (2), (3), and (4), respectively:

$$X_{Ethanol}(\%) = \frac{n_e - n_s}{n_e} * 100\% \tag{2}$$

$$Y_{Hydrogen} = \frac{n_{Hydrogen}}{n_e} \tag{3}$$

$$S_i(\%) = \frac{F_{P(i)}}{\sum F_{P(i)}} * 100\% \ or$$
$$S_i = \frac{n_i}{n_e - n_s} \tag{4}$$

where: n_e = moles of ethanol fed; n_s = moles of ethanol not converted during a 5 h reaction period; $n_{Hydrogen}$ = moles of hydrogen produced; n_i = moles of product; $F_{P(i)}$ = mean molar flow rate of product i produced (i = hydrogen, CO, CO_2, methane, acetaldehyde, or ethene); and $\sum F_{P(i)}$ = mean total molar flow rate of products i.

3 Results and Discussion

3.1 Catalyst Characterizations

3.1.1 N$_2$ Adsorption–Desorption Isotherms

Figure 1a shows the N_2 adsorption–desorption isotherms obtained for the SBA-15 support and the supported LaNiO$_3$ sample. The materials exhibited type IV isotherms, characteristic of mesoporous materials, according to the IUPAC classification. Sharp increases of the adsorbed volumes occurred in the relative pressure (P/P$_0$) ranges 10^{-5} to 10^{-2} and 0.5–0.8, for the support and the supported perovskite, corresponding to the filling of micropores and mesopores, respectively [28, 32]. This behavior could be explained by capillary condensation within the structured mesoporous material [27]. A hysteresis loop was observed for these materials, suggesting a difference between the processes of
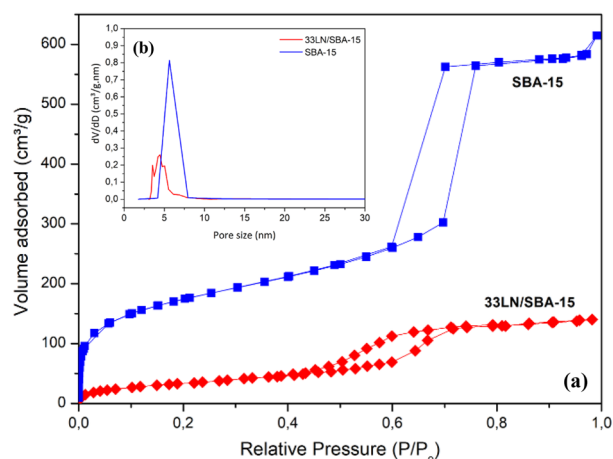

Fig. 1 Nitrogen adsorption and desorption isotherm curves (**a**) and pore size distributions (**b**) of the SBA-15 support material and the 33LN/SBA-15 supported perovskite

condensation and evaporation of the gas [24]. Comparison of these findings with those of other studies concerning supported perovskites confirmed that the SBA-15 mesoporous structures remained after addition of the active component and calcination [22, 24, 32, 33].

As shown in Fig. 1a, compared to SBA-15, the adsorption shifted to lower P/P$_0$ for the supported perovskite, with the hysteresis loop becoming smaller. At the same time, the pore size distribution (Fig. 1b) shifted to smaller sizes after the loading of LaNiO$_3$ on the SBA-15. The pore sizes were distributed uniformly in the range 4–8 nm for SBA-15 and in the range 3–6 nm for the supported LaNiO$_3$. The narrow distributions were characteristic of mesoporous SBA-15 silica. These observations were indicative of confinement of LaNiO$_3$ within the SBA-15 pores, leading to reductions of the BET surface area, pore volume, and mean pore size (Table 1). This was consistent with the findings of Wang et al. (2013), who showed that the textural properties of SBA-15 changed after formation of the perovskite structure on this silica matrix. This was attributed to anchoring of the LaNiO$_3$ particles in the SBA-15 pores, as revealed by TEM images showing the dispersion of perovskite within the pores of the support [24].

In this work, very low BET surface area (2.8 m^2 g^{-1}) was observed for the bulk LN perovskite (Table 1). According to the literature, the surface area of perovskite is generally < 10 m^2 g^{-1}, due to the high calcination temperature needed to form this structure [21]. In order to overcome these limitations and improve catalytic performance, a strategy is to disperse perovskite on materials with high surface area, such as SBA-15. The resulting increase in the perovskite specific surface area (Table 1) enables exposure of greater quantities of active sites to the reactants and gas-phase intermediates [31, 34].

Table 1 Characteristics of the materials: Ni content, BET surface area (S_{BET}), pore volume (V_P), and average pore size (D_p)

Sample	Ni (wt%)		S_{BET} (m^2 g^{-1})	V_P (cm^3 g^{-1})	D_P (nm)
	Theoretical	Experimental			
SBA-15	–	–	624	0.870	6.10
LN	23.9	26.1	2.8	–	–
33LN/SBA-15	7.9	8.8	131	0.250	4.46
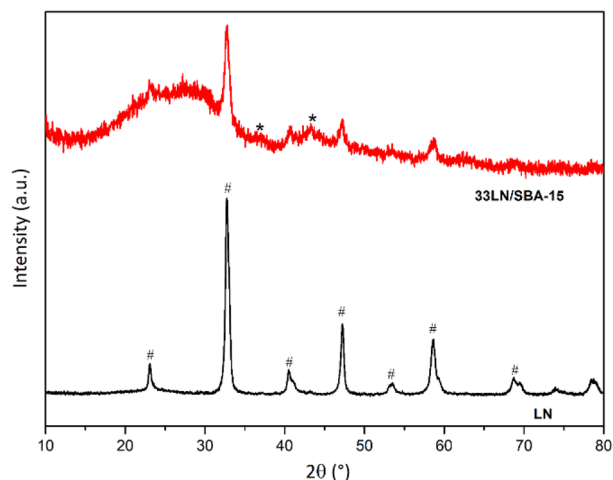
Fig. 2 X-ray diffraction patterns obtained for the calcined LN and 33LN/SBA-15 samples. #LaNiO$_3$ JCPDS 33-711; *NiO JCPDS 44-1159

The Ni contents of the catalysts, obtained by XRF analysis, are shown in Table 1. For both samples, the experimental compositions were close to the nominal values.

3.1.2 XRD and Morphological Analyses

The X-ray diffractograms of the bulk perovskite (LN) and the supported perovskite (33LN/SBA-15) are shown in Fig. 2. The diffraction patterns of the materials presented peaks characteristic of the LaNiO$_3$ phase (JCPDS 33-711). The diffractogram for the supported perovskite also showed peaks typical of the NiO phase (JCPDS 44-1159). No diffraction peaks corresponding to impurity phases such as NiO and La$_2$O$_3$ were observed for the bulk perovskite, indicating formation of the pure LaNiO$_3$ perovskite phase. The NiO impurity phase can arise from high dispersion of oxide phases on mesoporous materials, which can hinder formation of the LaNiO$_3$ perovskite phase in the calcination step by the reaction between NiO and La$_2$O$_3$. Similar results for LaNiO$_3$ supported on SBA-15 mesoporous silica were reported by Wang et al. [24] and Rivas et al. [32].

The broad peak centered at 27.5° (Fig. 2) was associated with the amorphous pore wall feature of pure SBA-15 silica. The SBA-15 support only presented low-angle diffraction peaks, which could be explained by the well-developed structure with ordered hexagonal pores, providing long-range order. Figure 3a shows the low-angle diffractograms for the support material and the supported 33LN/SBA-15 catalyst. The two well-resolved characteristic peaks could
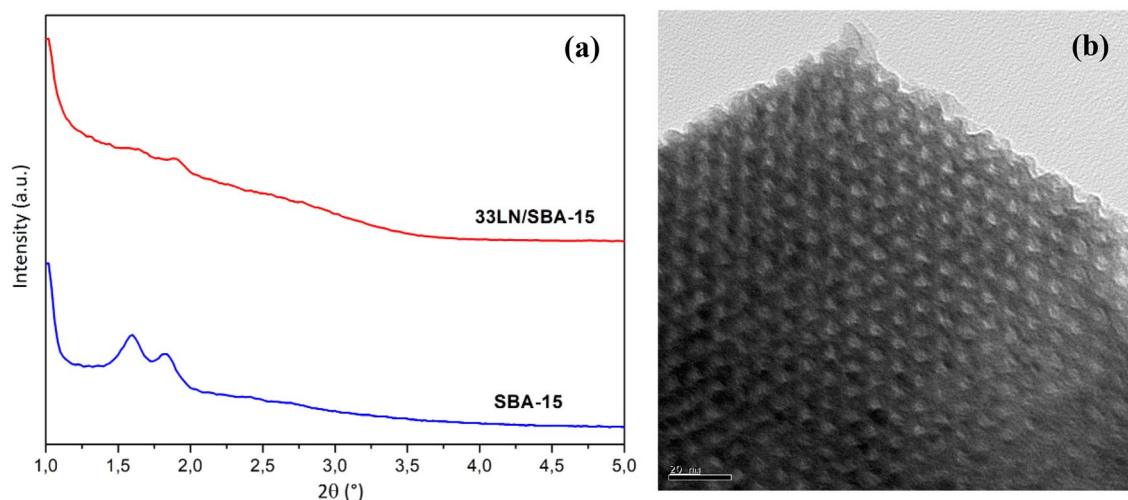

Fig. 3 **a** Low-angle X-ray diffractograms of SBA-15 and the supported 33LN/SBA-15 catalyst, and **b** TEM image of the SBA-15 sample after calcination

be assigned to diffraction planes (110) and (200) of SBA-15. The main peak [plane (100)] of SBA-15 is only observed in 2θ values less than 1°. In this work, this peak was not identified in the diffractogram of SBA-15, because the limitations of the equipment for angles smaller than 1°. Figure 3b shows the highly ordered mesoporous structure of SBA-15, providing confirmation of the formation of this silica. The loading with $LaNiO_3$ significantly influenced the SBA-15 pore structure. The diffraction peaks for 33LN/SBA-15 showed considerably lower intensity, which could be explained by partial blocking of the mesopores and decreased long-range order of the hexagonal arrangement. These results were in agreement with the adsorption–desorption isotherms for the perovskite-type oxides loaded on SBA-15 (Fig. 1, Table 1), which indicated dispersion of this structure within the mesopores of the support. Similar results were reported by Albuquerque et al. (2008) for CaO supported on mesoporous silica, where the intensities of the diffraction peaks corresponding to the hexagonal structure decreased after loading of the oxide phase on the support [35].

The use of SEM was important for elucidation of the morphologies and microstructures of the synthesized catalysts. Figure 4a shows the microstructure of LN after calcination, with the presence of grains. It is known that sol–gel methods lead to the formation of perovskites with fine and uniform grains. SBA-15 rods with meso-channels were clearly present for the 33LN/SBA-15 sample (Fig. 4b), indicating that the long-range structural order of SBA-15 was retained after loading with $LaNiO_3$.

The low-angle XRD and SEM analyses suggested that the structure of the SBA-15 support remained after loading and calcination at 750 °C, which could be attributed to the inherent good thermal stability of SBA-15 [24, 36]. The pore wall thickness for SBA-15 prepared with P123 is estimated

to be 3.1 nm. These wall structures are much thicker, compared to those typically obtained using MCM-41 (around 10 to 15 Å), with cationic alkylammonium surfactant species as structure-directing agents. Therefore, SBA-15 shows improved stability at high temperatures or during longer reaction times, compared to MCM-41 [27, 36].

3.1.3 Reducibility of the Catalysts

The H_2-TPR profiles of the materials, the bulk $LaNiO_3$ perovskite, and the $LaNiO_3$ perovskite supported on SBA-15 are shown in Fig. 5. The LN reduction profile showed a peak centered at 361 °C, with a shoulder at 364 °C, and a second peak centered at 485 °C. The first peak at 361 °C could be attributed to the reduction of Ni^{3+} to Ni^{2+}, while the second
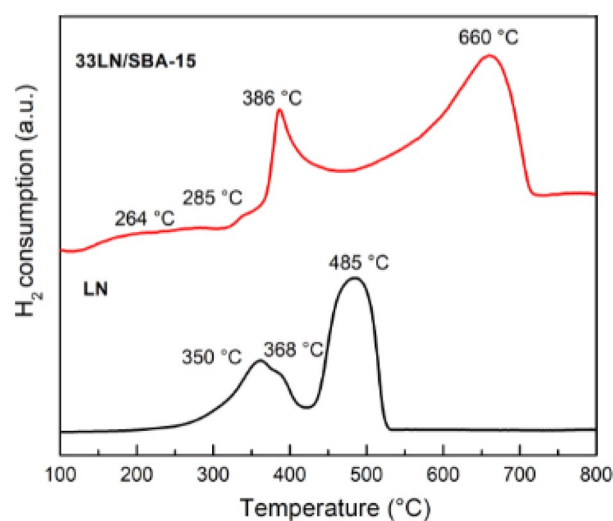
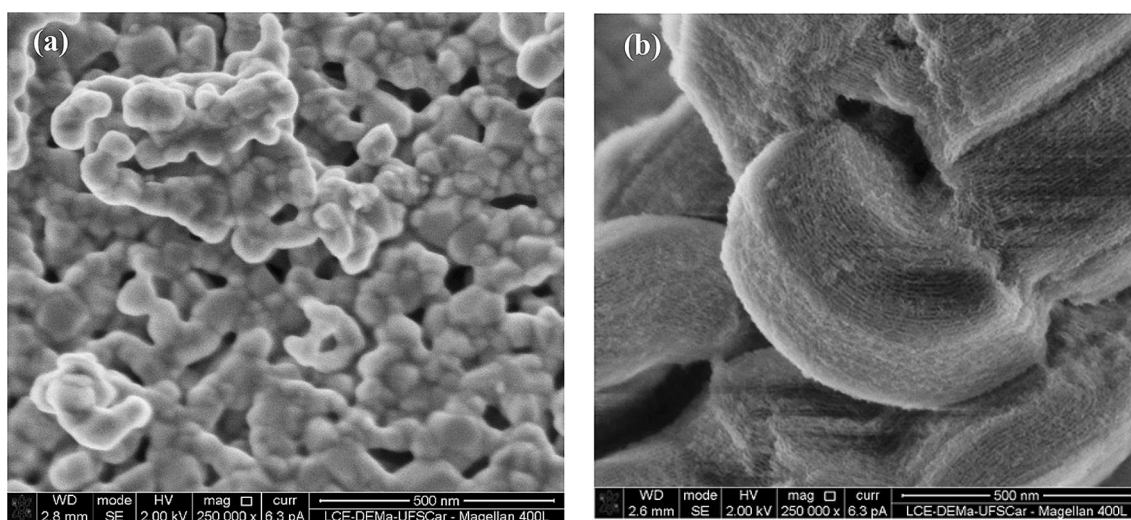**Fig. 5** TPR profiles of the calcined LN and 33LN/SBA-15 catalysts

Fig. 4 SEM images of **a** LN and **b** 33LN/SBA-15, after calcination

peak at 485 °C corresponded to the reduction of Ni^{2+} to Ni^0, with both peaks related to the perovskite structure. The shoulder peak at 364 °C was due to the reduction of Ni^{2+} to Ni^0, for the nickel oxide (NiO) from the Ni that was not a constituent of the perovskite structure. Similar reduction steps were reported by De Lima et al. (2010) for bulk $LaNiO_3$ perovskite, where the shoulder peak was attributed to reduction of an NiO impurity phase that was undetected by XRD, suggesting the possible presence of well-dispersed particles of NiO in the material [14].

This two-step reduction process of the bulk perovskite indicated formation of the intermediate $La_2Ni_2O_5$ species, as follows [14, 30, 37]:

$$LaNiO_3 + H_2 \rightarrow La_2Ni_2O_5 + H_2O \tag{5}$$
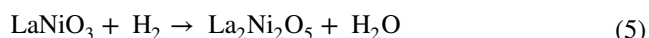
The second step involved complete reduction of perovskite to La_2O_3 and Ni^0:

$$La_2Ni_2O_5 + 2H_2 \rightarrow 2Ni^0 + La_2O_3 + 2H_2O \tag{6}$$
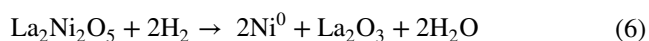
The hydrogen consumption values for the bulk and supported $LaNiO_3$ materials are provided in Table 2. A value of 2 for the ratio of the area of the second peak to that of the first peak generally indicates that the first reduction step is the formation of Ni^{2+}, which is then reduced to Ni^0. In the case of LN, the hydrogen consumption during the first step was approximately 1/3 of the consumption during the second step. This ratio corresponded to the formation of Ni^0 from the impurity NiO phase during the first stage of the reduction, in agreement with previous reports [14, 38], where the shoulder peak at 368 °C was attributed to reduction of the NiO particles.

Compared to the bulk perovskite, reduction of the supported perovskite showed a substantial shift towards higher temperatures, with broadening of the signal. A likely explanation for this difference in the TPR profiles was decrease of the particle size, from bulk material to ultrafine particles [24, 32]. Additionally, a shoulder peak between 100 and 350 °C observed for the supported $LaNiO_3$ catalyst could be attributed to nickel oxide (NiO), while the other peaks corresponded to reduction of $LaNiO_3$. An earlier study also

reported reduction of nickel oxide supported on SBA-15 in this temperature range (127–347 °C) [38]. The NiO phase could have originated from the Ni precursor salt that did not contribute to the perovskite structure during the synthesis [14, 39].

The NiO phase could also be attributed to the ease of insertion of metal cations into the perovskite structure. In the study by Xiao et al. (2014), the X-ray diffractogram of $LaCoO_3$/SBA-15 showed the formation of pure perovskite phase. Since Co has a smaller ionic radius than Ni, the perovskite structural arrangement is more easily formed with this metal. In addition, the tolerance factor (t) is closer to 1, indicating the formation of a perovskite structure that is more stable [17, 33].

As can be seen in the information summarized in Table 2, the loading with $LaNiO_3$ led to identification of a fourth reduction zone (530–715 °C), together with substantial decreases of the peak percentages for the third reduction zone (425–530 °C). Therefore, the third peak between 450 and 550 °C for the supported perovskite could be explained by the reduction of segregated perovskite $LaNiO_3$ particles, which could be observed by comparing the reduction profile to that of the bulk perovskite. This showed the positive influence of the support in dispersion of the $LaNiO_3$ particles.

In summary, the reduction steps of the supported perovskite were similar to the features observed for the bulk perovskite. The TPR experiments demonstrated that formation of the active sites (metallic nickel) for the ethanol steam reforming occurred during the reduction step. This indicated that the perovskite structure was destroyed after reduction at 750 °C, with Ni^0 particles being deposited over the lanthanum oxide.

3.1.4 Nickel Particle Size and Metallic Area

The TPR experiments showed the formation of active sites (metallic nickel) for ethanol steam reforming during the reduction step. The X-ray diffractograms of the reduced materials are provided in Fig. 6. The $LaNiO_3$ and $LaNiO_3$/SBA-15 diffractograms showed the presence of metallic phases of Ni at 2θ of ~ 44.5°, as well as La_2O_3. For the supported perovskite, the diffraction peaks of La_2O_3 were of low intensity, which could be explained by the dispersion of the La_2O_3 on the SBA-15.

The Ni crystallite size was estimated from the X-ray line broadening, applying the Scherrer equation. The average metallic Ni crystallite sizes were 7.6 and 2.0 nm for LN and 33LN/SBA-15, respectively (Table 3), showing that use of the SBA-15 support resulted in a substantial decrease of the Ni crystallite size, compared to the bulk perovskite, indicating that the $LaNiO_3$ was highly dispersed on the SBA-15 [22].

Table 2 H_2 consumption according to deconvoluted TPR region

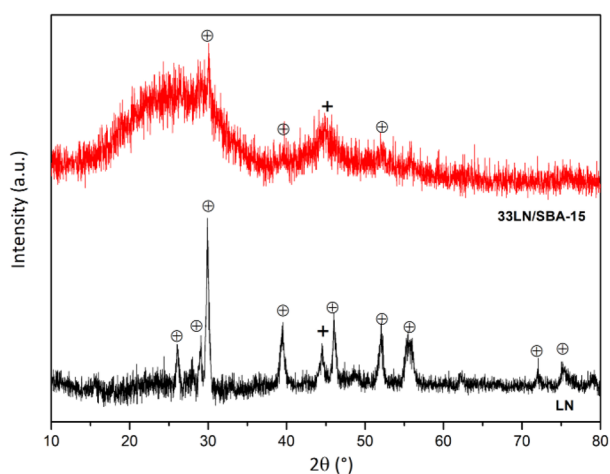| Sample	H_2 consumption (%)			
	First peak (100–350 °C)	Second peak (350–425 °C)	Third peak (425–530 °C)	Fourth peak (530–715 °C)
LN	–	40	60	–
33LN/SBA-15	5.50	33.8	12.4	48.3

Fig. 6 X-ray diffractograms obtained for LN and 33LN/SBA-15 after reduction. (⊗) La$_2$O$_3$; (+) Ni

Table 3 Crystal sizes after reduction (nm), metallic areas (m^2 g$_{Ni}^{-1}$), ethanol conversions (%), and crystal sizes after stability testing (nm)

Sample	d$_{Ni}$ (nm)[a]		Metallic area (m^2 g$_{Ni}^{-1}$)	Conversion (%)	d$_{Ni}$ (nm)[a] (after reaction)
	XRD[a]	TEM			
LN	7.6	7.7 ± 1.9	1.2	78	11.4
33LN/SBA-15	2.0	2.2 ± 0.3	3.9	99	2.4

[a]Calculated using the Scherrer equation and the characteristic Ni (111) line at 2θ = 44.5°, after reduction at 750 °C

The morphological features of the reduced catalysts were investigated using TEM. Representative images of LN and 30LN/SBA-15 after reduction are shown in Figs. 7 and 8, respectively. The darker regions in the images correspond to the Ni particles with different sizes. The TEM images of 33LN/SBA-15 (Fig. 8) revealed that the long-range order of SBA-15 was maintained after the reduction. The small dark spots in area I could be attributed to Ni particles located in the channels of the support. Larger dark spots over the pores in area II are due to some agglomerated particles on the external surface, formed by migration of the perovskite species out of the support during calcination [22, 24].

The sizes of Ni particles, estimated by TEM, were around 7.7 nm for LN (Fig. 7b) and 2.2 nm for 33LN/SBA-15 (Fig. 8b), which were in agreement with the XRD results (Table 3). For 33LN/SBA-15, the Ni particles were in the size range 1–4 nm (Fig. 8b), with the size distribution being narrower, compared to LN. The metallic area results for LN and 30LN/SBA-15 after reduction are shown in Table 3. The metallic area of the Ni nanoparticles was higher for 33LN/SBA-15, indicating that the nickel catalyst prepared from LaNiO$_3$/SBA-15 provided higher dispersion of nickel after

reduction, in agreement with the particle sizes indicated by the XRD and TEM analyses.

3.2 Catalytic Performance in Ethanol Steam Reforming

Evaluation of the activities of Ni catalysts prepared from LaNiO$_3$ and LaNiO$_3$ supported on SBA-15 was first performed using the ethanol steam reforming reaction at 500 °C, with H$_2$O/ethanol molar ratio of 3.0, and N$_2$ as the carrier gas. The ethanol conversions obtained for LaNiO$_3$ and LaNiO$_3$ supported on SBA-15 were 78 and 99%, respectively (Table 3). The hydrogen yields obtained using LN and 33LN/SBA-15, according to time on stream, are shown in Fig. 9. As shown in Table 3, the ethanol conversion increased with the perovskite loading on the support, which explained the higher hydrogen yield shown in Fig. 9. Besides being more active, the performance of the 33LN/SBA-15 catalyst remained almost constant with time on stream. The hydrogen yield followed the same trend for both catalysts, increasing at the start of the reaction and then remaining constant at around 2.7 and 3.8 mol H$_2$ mol^{-1} ethanol for LN and 33LN/SBA-15, respectively, although a decrease after 60 min was observed for LN.

The experimental results showed that the SBA-15 support had a significant effect on the Ni particle size, as shown by the XRD and TEM analyses. Dispersion of the active phase on the support resulted in a smaller size of the metallic Ni particles on 33LN/SBA-15 during the reduction. Therefore, the higher activity of 33LN/SBA-15 in the reaction could be explained by the greater nickel dispersion, as shown by the metallic area, which increased the quantity of active sites available to the reactants and the gas-phase intermediates.

The results of the catalytic assays, together with the Ni particle size data, suggested that the agglomeration of nickel species was hindered by the presence of the mesoporous support. The higher stability observed for 33LN/SBA-15 could have been associated with the better dispersion of the particles, compared to the LN catalyst that showed a decrease of the hydrogen yield after 60 min of reaction. Hence, greater dispersion acted to reduce the possibility of catalyst deactivation by nickel sintering. Similar features concerning the influence of particle size on catalytic performance have been reported previously. Wang et al. (2013) studied the properties of Ni perovskite catalysts supported on SBA-15 and MCM-41, used in the dry reforming of CH$_4$. Higher dispersion of the Ni particles on SBA-15 was suggested to be the main reason for stabilization of the metallic particles, avoiding agglomeration and maintaining catalytic performance [24].

Similar behavior was reported by Rabelo-Neto et al. (2018) for the performance of Ni catalysts obtained using LaNiO$_3$, LaNiO$_3$/Al$_2$O$_3$, and LaNiO$_3$/CeSiO$_2$, which were
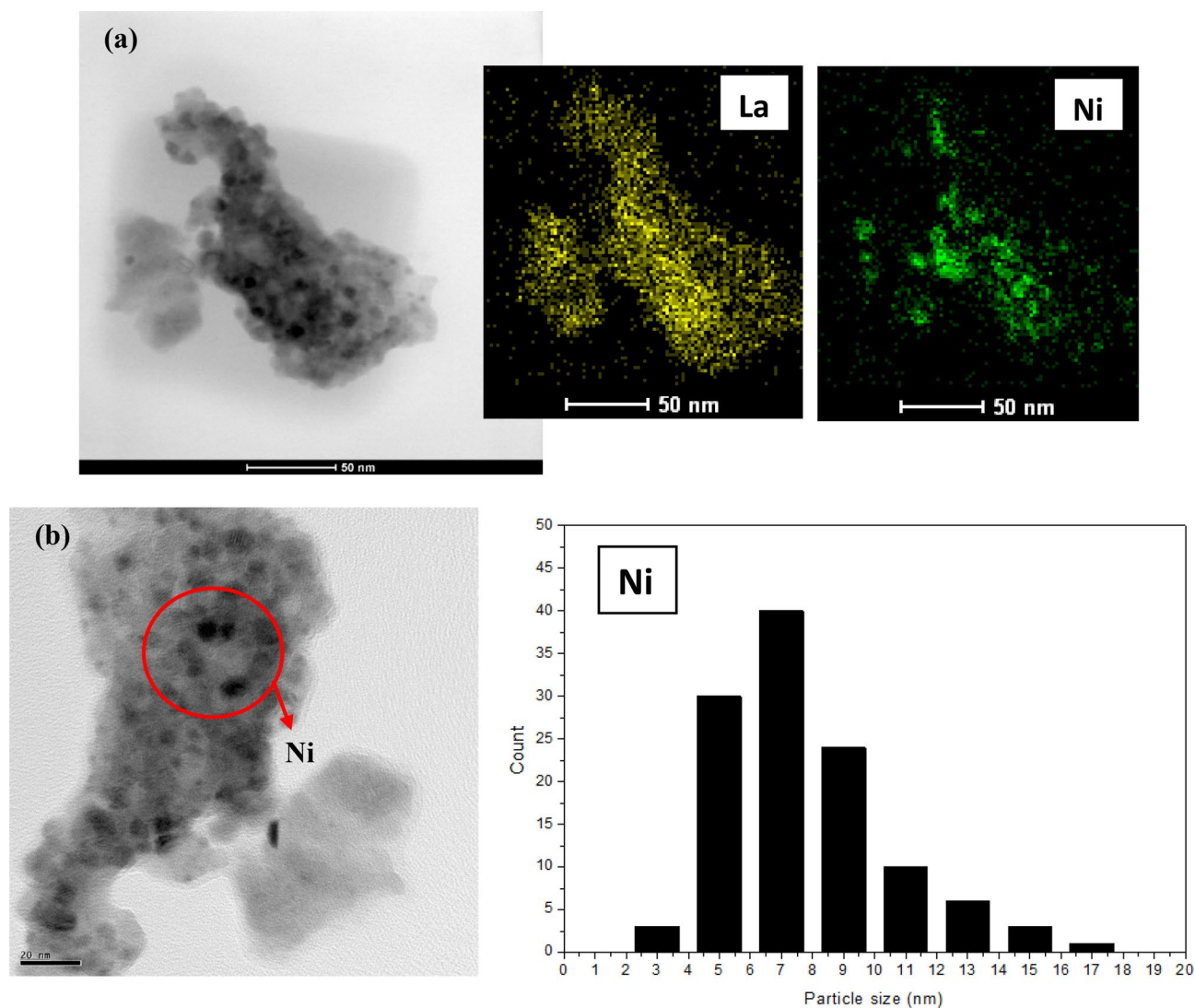
Fig. 7 TEM image and element mapping (**a**) and particle size distribution (**b**) for the LN catalyst after reduction

employed in the methane dry reforming reaction, with higher initial reaction rates observed for the supported perovskites. In addition, the dispersion of Ni was higher for these supported catalysts, compared to the unsupported ones [34]. Hence, similarly, greater dispersion of nickel provided an explanation for the higher activity of 33LN/SBA-15.

A similar or higher specific activity (Ni mass normalized activity) was observed in the supported material compared to literature results. The hydrogen yield obtained in this work with 33LN/SBA-15 was similar to the yields reported by other authors using silica-supported Ni catalysts [37, 40] (Table 4). However, here it was possible to obtain this similar yield at lower temperatures and with stoichiometric H_2O feeding, in addition to higher specific activity. These observations highlight the importance of the synthesis method proposed in this work to obtain Ni catalysts from perovskites supported on mesoporous silica, with an

improved yield of H_2 reached using Ni/La_2O_3 obtained from $LaNiO_3$. Figure 10 shows the selectivity results for all the products during the five-hour stability test. The only products detected were hydrogen, CO, CO_2, and CH_4. Superior H_2 and CO_2 selectivity provided by 33LN could be explained by the highest rate of decomposition of the dehydrogenated species, producing H_2, CO, and CH_x species, as well as the highest reaction rate for conversion of CO to CO_2. The lower CH_4 selectivity presented by LN could be attributed to faster formation of CH_x species, relative to the rate of desorption of these species in the form of CH_4. Further dehydrogenation of the CH_x species could lead to the formation of H and C. Similar results were reported by Marinho et al. (2016) for ethanol steam reforming using Ni catalysts produced from bulk and supported $LaNiO_3$ perovskites [25].

Table 5 provides a comparison of catalytic activity in ethanol steam reforming for nickel-based materials
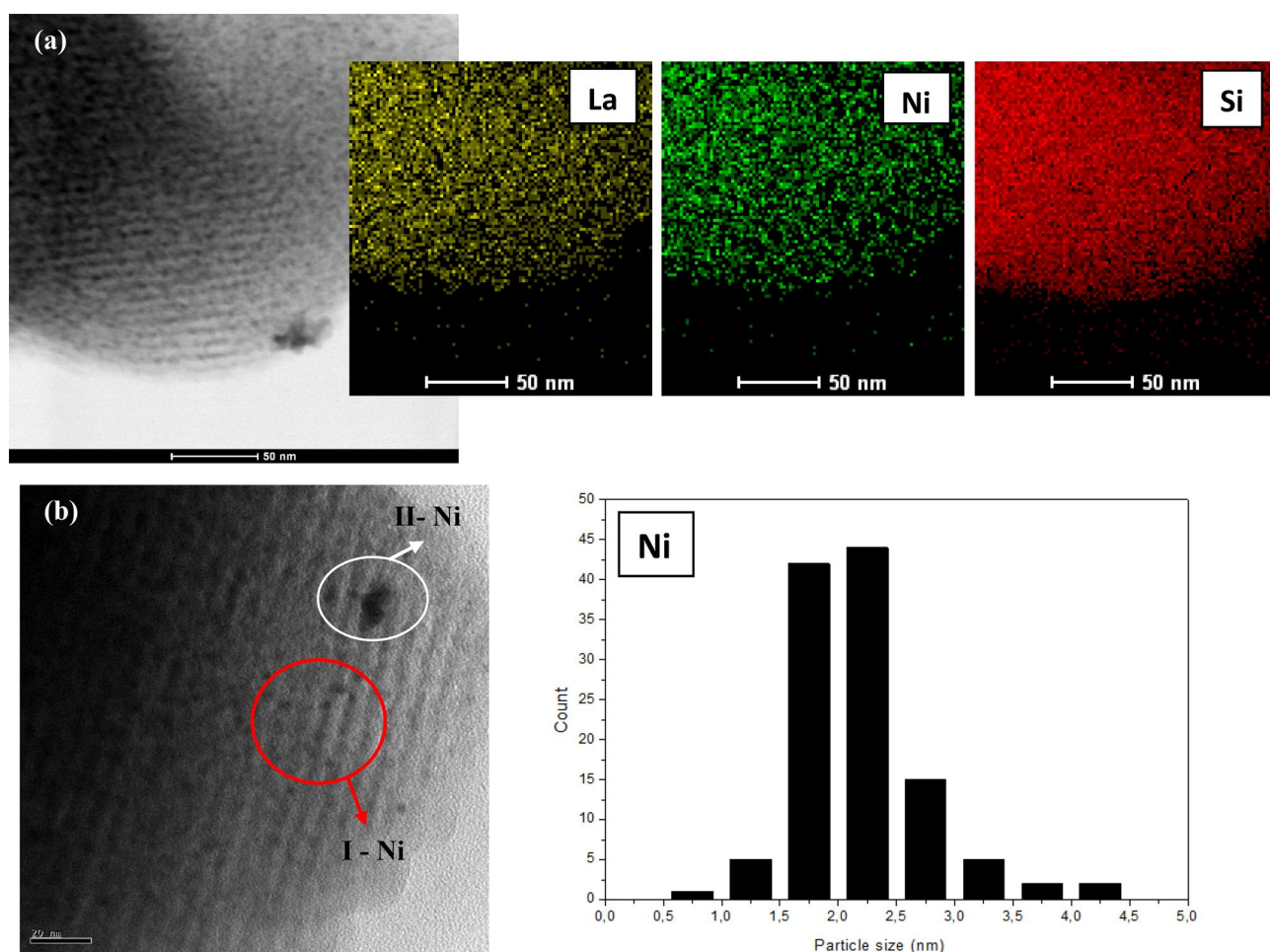
Fig. 8 TEM image and element mapping (**a**) and particle size distribution (**b**) for the 33LN/SBA-15 catalyst after reduction
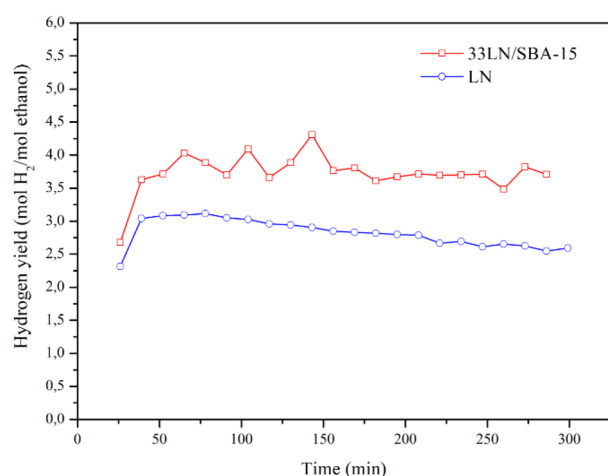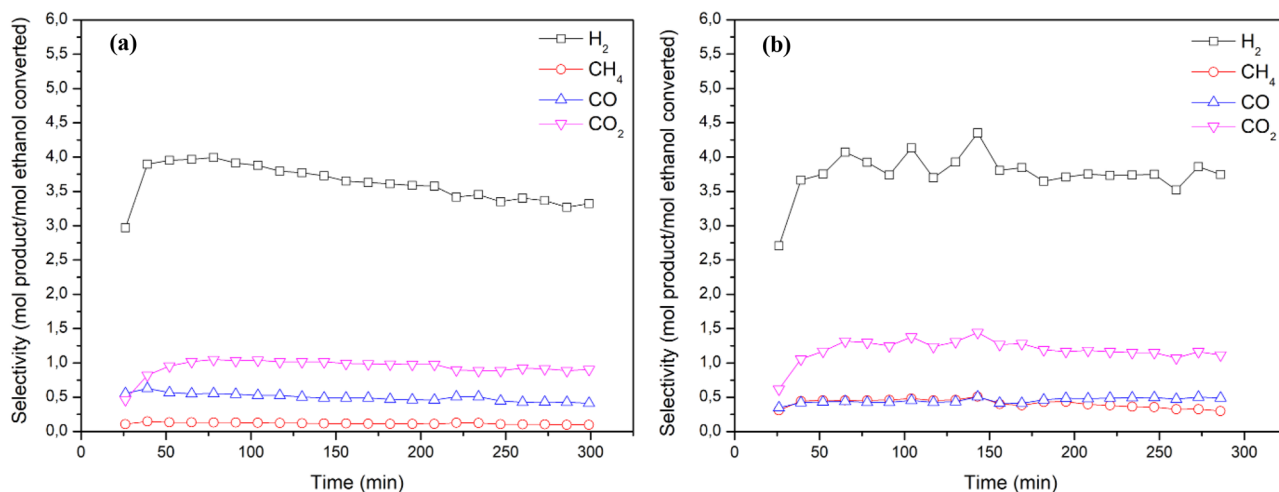

Fig. 9 Hydrogen yield versus time on stream, for ethanol steam reforming at 550 °C, with H_2O/ethanol molar ratio of 3.0, using the Ni catalysts obtained from bulk perovskite (LN) and supported perovskite (33LN/SBA-15)

derived from perovskite and supported on mesoporous silicas such as SBA-15 or disordered silicas [25, 30, 41, 42]. The different results can be explained by the natures of the catalysts (obtained using different synthesis methods) and the operating conditions. Comparing the results obtained in this work to those reported elsewhere (Table 5), it can be seen that the conversions achieved using 33LN/SBA-15 were similar to those for materials supported on silica, but higher than those obtained using $LaNiO_3$ and $LaNiO_3/CeSiO_2$. Furthermore, 33LN/SBA-15 presented higher selectivity to H_2, compared to the nickel catalysts $LaNiO_3/ZrO_2$ and Ni/SiO_2. These results confirmed the efficiency of Ni catalysts obtained from perovskite supported on SBA-15, which combined greater $Ni–La_2O_3$ interaction from the reduction of perovskite [37] with dispersion in a mesoporous structure presenting high specific area.

The main problem encountered during ethanol reforming is deactivation of the catalyst. The crucial effect of the supported perovskite on avoidance of carbon deposition on

Table 4 Comparison of Ni mass normalized activity and hydrogen yields obtained in the present work and in studies reported in the literature for the steam reforming of ethanol

Catalysts	Reaction conditions	Ni mass normalized Activity (mol/h/g nickel)	H_2 yield (mol H_2 per mol ethanol fed)	References
Ni/SiO$_2$	Temperature 500 °C H$_2$O/ethanol (molar ratio)=6	0.136	3.5	[37]
CuNi–La20SBA	Temperature 600 ºC H$_2$O/ethanol (molar ratio)=3.7	1.64	3.8	[40]
6Ni/SBA-15(C)	Temperature 550 °C H$_2$O/ethanol (molar ratio)=3	0.890	4.8	[41]
Ni(2)7.5SBA-15	Temperature 550 °C H$_2$O/ethanol (molar ratio)=6	0.318	–	[42]
Cu$_2$Ni$_7$/SBA-15 (WI)	Temperature 600 °C H$_2$O/ethanol (molar ratio)=3.7	1.74	3.2	[43]
6Ni-1.2Au/SBA-15 6Ni/SBA-15	Temperature 550 °C H$_2$O/ethanol (molar ratio)=3	0.911 0.966	4.8 4.0	[44]
LN (LaNiO$_3$) 33LN/SBA-15 (LaNiO$_3$/SBA-15)	Temperature 550 ºC H$_2$O/ethanol (molar ratio)=3 Average of 5 h	1.37 1.70	2.8 3.6	This work This work

Fig. 10 Selectivity of products versus time on stream for ethanol steam reforming at 550 °C, with H$_2$O/ethanol molar ratio of 3.0, using the Ni catalysts obtained from bulk perovskite (LN) (**a**) and supported perovskite (33LN/SBA-15) (**b**)

the catalyst was demonstrated in stability tests performed for ethanol steam reforming without use of the N$_2$ carrier gas. The conversion values and average selectivities for all

the products obtained during the five-hour stability test are shown in Table 6. Similar conversions were observed for the LN and 33LN/SBA-15 samples. The main products formed

Table 5 Performance comparison of Ni-based catalysts used in the steam reforming of ethanol

Catalysts	Operating conditions (steam reforming of ethanol)	$X_{Ethanol}$ (%)	Mean selectivity to products	References
LaNiO$_3$ 23.0 wt% Ni	Temperature 500 °C H$_2$O/ethanol (molar ratio) = 3 GHSV 200,000 mL g$_{cat}^{-1}$ h^{-1}	97 *(initial ethanol conversion)* 70 and 60 *(after 5 h and 22 h of reaction, respectively)*	H$_2$ (68%) CO$_2$ (20%) CO (10%) CH$_4$ (2%)	[25]
Ni/SiO$_2$ 9.3 wt% Ni	Temperature 500 °C H$_2$O/ethanol (molar ratio) = 3 GHSV 48,500 mL g$_{cat}^{-1}$ h^{-1}	100	H$_2$ (54%) CO$_2$ (23%) CO (6%) CH$_4$ (17%)	[45]
6Ni/SBA-15(C) 6 wt% Ni	Temperature 550 °C H$_2$O/ethanol (molar ratio) = 3 GHSV 27,450 mL g$_{cat}^{-1}$ h^{-1}	100	H$_2$ (66%) CO$_2$ (17%) CO (13%) CH$_4$ (4%)	[41]
LaNiO$_3$/CeSiO$_2$ 6.9 wt% Ni	Temperature 500 °C H$_2$O/ethanol (molar ratio) = 3 GHSV 59,701 mL g$_{cat}^{-1}$ h^{-1}	85 *(initial ethanol conversion)* 70 and 60 *(after 5 h and 22 h of reaction, respectively)*	H$_2$ (69%) CO$_2$ (20%) CO (6%) CH$_4$ (5%)	[25]
LaNiO$_3$/ZrO$_2$ 5.4 wt% Ni	Temperature 550 °C H$_2$O/ethanol (molar ratio) = 3 GHSV 66,000 mL g$_{cat}^{-1}$ h^{-1}	100%	H$_2$ (58%) CO$_2$ (20%) CO (13%) CH$_4$ (9%)	[30]
LN (LaNiO$_3$) 26.1 wt% Ni 33LN/SBA-15 (LaNiO3/SBA-15) 8.8 wt% Ni	Temperature 550 °C H$_2$O/ethanol (molar ratio) = 3 GHSV (LN) and (33LN/SBA-15) ~850,000 mL g$_{Ni}^{-1}$ h^{-1} (LN) 224,318 mL g$_{cat}^{-1}$ h^{-1} (33LN/SBA-15) GHSV 74,025 mL g$_{cat}^{-1}$ h^{-1}	78% Average of 5 h

99% Average of 5 h | H$_2$ (70%) CO$_2$ (18%) CO (13%) CH$_4$ (2%)

H$_2$ (65%) CO$_2$ (20%) CO (8%) CH$_4$ (7%) | This work

This work |

Table 6 Catalytic performance of the catalysts obtained from the bulk and supported perovskite during stability testing for 5 h in the ethanol steam reforming reaction, without use of the N$_2$ carrier gas

Catalyst	Conversion (%)	Selectivity (%)						CO$_2$/CO ratio
		H$_2$	CH$_4$	CO	CO$_2$	C$_2$H$_4$	C$_2$H$_4$O	
LN	90	63.2	10.7	10.1	15.8	0.2	0	1.6
33LN/SBA-15	92	62.4	10.7	7.4	19.5	0	0.1	2.6

were H$_2$, CO, CO$_2$, and CH$_4$. Small quantities of ethylene and acetaldehyde were also detected over the supported LN catalyst and 33LN/SBA-15, respectively.

Comparison of the conversions obtained in the catalytic tests carried out under different conditions showed that at low feed rates, similar conversions were obtained for LN and

33LN/SBA-15. However, with increase of the gas flow (from the N_2 feed), the 33LN/SBA-15 catalyst provided higher conversion, indicative of a higher reaction rate, which could be explained by the greater active surface of this catalyst.

Considering the products observed in the reaction tests (Fig. 10 and Table 4), the following steps could be proposed for the ethanol steam reforming using the catalysts studied:
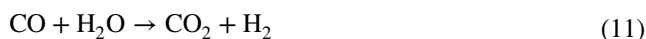
(1) Ethanol dehydrogenation:

$$C_2H_5OH \rightarrow C_2H_4O + H_2 \tag{7}$$

(2) Steam reforming of acetaldehyde:

$$C_2H_4O + H_2O \rightarrow CH_4 + CO_2 + H_2 \tag{8}$$
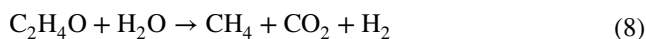
(3) Acetaldehyde decomposition

$$C_2H_4O \rightarrow CH_4 + CO \tag{9}$$

(4) Methane steam reforming:

$$CH_4 + H_2O \rightarrow CO + 3H_2 \tag{10}$$

(5) Water gas shift reaction

$$CO + H_2O \rightarrow CO_2 + H_2 \tag{11}$$

In the other direction:
(6) Ethanol dehydration

$$C_2H_5OH \rightarrow C_2H_4 + H_2O \tag{13}$$

(7) Aldolic condensation, followed by dehydrogenation

$$2C_2H_5OH + H_2O \rightarrow CH_3COCH_3 + CO_2 + 4H_2 \tag{14}$$

Steps 6 and 7 lead to species that are precursors of coke formation. Similar pathways have been proposed previously for ethanol steam reforming using perovskite Ni catalysts [30, 37]. De Lima et al. (2010) investigated the mechanism for ethanol reforming over perovskite Ni catalysts, using in situ DRIFTS experiments [14]. In the proposed reaction mechanism, decomposition of the dehydrogenated species produced H_2, CO, and CH_x species, which could then lead to carbon formation, depending on the hydrogen recombination rate. This carbon could react with water, or remain on the surface of the material, causing encapsulation of the nickel metal particles and catalyst deactivation.

Figure 11 shows the weight losses of LN and 33LN/SBA-15 after reaction, determined by TGA. The greatest carbon formation was shown by $LaNiO_3$. SEM images of the catalysts after reaction (Fig. 12) revealed a large quantity of filamentous carbon over the LN catalyst, while a smaller amount of this type of carbon was detected on the 33LN/SBA-15 catalyst, demonstrating that use of the supported $LaNiO_3$ resulted in significantly lower carbon deposition.

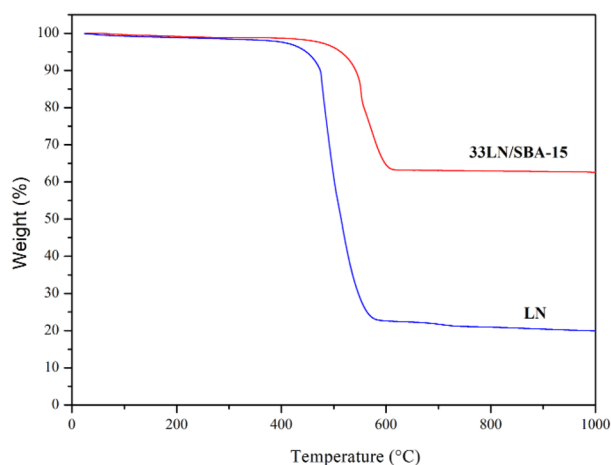The XRD and TEM analyses showed that the presence of SBA-15 support had a major influence on the Ni

Fig. 11 TGA results for the used LN and 33LN/SBA-15 catalysts after stability testing in the ethanol steam reforming reaction, without use of the N_2 carrier gas, at 550 °C, with H_2O/ethanol molar ratio of 3.0

crystallite size. For 33LN/SBA-15, the Ni particle size was threefold smaller, compared to the unsupported catalyst. This contributed to the lowest amount of carbon formed on the 33LN/SBA-15 catalyst, in agreement with results reported in the literature. Additionally, as shown in Table 6, the ethanol conversions and selectivities for H_2 and CH_4 were approximately the same for the two catalysts. Therefore, the increase of the CO_2/CO ratio for the supported catalysts could be associated with the improved resistance to carbon deposition. This ratio depends on the WGSR, so a higher CO_2/CO ratio indicates higher ability to activate water, favoring carbon removal reactions [30].

Marinho et al. (2016) also reported lower initial conversion for a catalyst obtained from $LaNiO_3$ perovskite supported on $CeSiO_2$, compared to a catalyst obtained from bulk $LaNiO_3$ perovskite [25]. However, a lower carbon formation rate was observed for the supported catalyst. The Ni^0 size has a significant effect on carbon formation, because smaller crystallite size hinders the initiation step for carbon formation over metal particles [10, 20].

Table 7 shows the amounts of carbon formed during the steam reforming of ethanol, observed in this work and for different Ni-based catalysts reported in the literature [30, 37, 42–44]. The Ni catalyst obtained from $LaNiO_3$ supported on SBA-15 (33LN/SBA-15) showed a lower rate of carbon formation, compared to materials supported on silica and SBA-15 (about 50% lower than for some of the other catalysts). Hence, the results obtained here demonstrated the effectiveness of the method employed to obtain Ni catalysts with considerable potential for use in the steam reforming of ethanol.
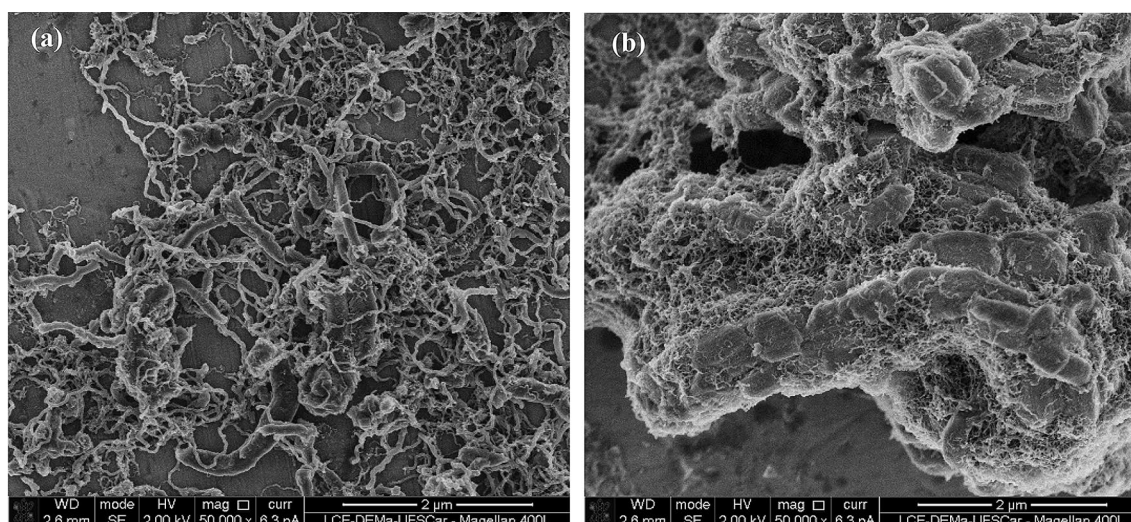
Fig. 12 SEM images of **a** LN and **b** 33LN/SBA-15 after stability testing in the ethanol steam reforming reaction, without use of the N_2 carrier gas

Table 7 Carbon formation in the ethanol steam reforming reaction for Ni catalysts reported in the literature and the catalysts studied in this work

Catalyst	Reaction conditions	TG (%) or amount of coke (mg g_{cat}^{-1} h^{-1})	References
Ni/SiO$_2$	Reaction at 395 °C for 14 h H$_2$O/ethanol (molar ratio) = 6 GHSV = 94,950 mL g_{cat}^{-1} h^{-1}	57.8%	[37]
6Ni/SBA-15(C)	Reaction at 550 °C for 25 h H$_2$O/ethanol (molar ratio) = 3 GHSV = 27,450 mL g_{cat}^{-1} h^{-1}	~33%	[41]
LaNiO$_3$/ZrO$_2$	Reaction at 650 °C for 50 h H$_2$O/ethanol (molar ratio) = 3 GHSV = 264,000 mL g_{cat}^{-1} h^{-1}	50%	[30]
10%Ni/SiO$_2$	Reaction at 500 °C for 4 h H$_2$O/ethanol (molar ratio) = 3 GHSV = 73,500 mL g_{cat}^{-1} h^{-1}	169 mg g_{cat}^{-1} h^{-1}	[46]
Ni@Zr-SBA-15	Reaction at 550 °C for 5 h H$_2$O/ethanol (molar ratio) = 3.2 GHSV = 20,000 mL g_{cat}^{-1} h^{-1}	152 mg g_{cat}^{-1} h^{-1}	[47]
LaNiO$_3$	Reaction at 550 °C for 5 h H$_2$O/ethanol (molar ratio) = 3 GHSV (LN) and (33LN/SBA-15)	539 (mg$_{carbon}$ g_{cat}^{-1} h^{-1}) or 75%	This work
LaNiO3/SBA-15	~ 160,000 mL g_{Ni}^{-1} h^{-1} *(LN)* 42,500 mL g_{cat}^{-1} h^{-1} (33LN/SBA-15) 14,025 mL g_{cat}^{-1} h^{-1}	109 (mg$_{carbon}$ g_{cat}^{-1} h^{-1}) or 37%	This work

4 Conclusions

Overall, the catalysts obtained from supported LaNiO$_3$ perovskite were found to be highly promising for applications involving ethanol steam reforming. The LaNiO$_3$ perovskite was successfully formed on mesoporous SBA-15 silica. The 33LN/SBA-15 catalyst was the most active in the reaction and presented the greatest stability during use. The superior activity of this material could be attributed to the better perovskite dispersion on SBA-15,

which increased the quantity of active sites available to the reactants. Dispersion of the perovskite on the support resulted in a smaller size of the metallic Ni particles on 33LN/SBA-15, compared to the LN catalyst derived from bulk LaNiO$_3$ perovskite, which increased the resistance to carbon deposition, since a smaller crystallite size hindered the initiation step for the formation of carbon over the metal particles. Hence, this effect can contribute to improving catalyst stability during ethanol steam reforming. Supported perovskites show considerable promise for the production of a wide range of other catalysts. In summary, catalysts derived from these supported oxides have advantages over those obtained from unsupported perovskite, including a higher surface area available for contact between the perovskite and the reactants, as well as higher stability due to decreased carbon formation.

Declarations

Conflict of interest The authors declare that there is no conflict of interests regarding the publication of this article.

References

1. CGEE (2010) Hidrogênio energético no Brasil: subsídios para políticas de competitividade, 2010–2025; Tecnologias críticas e sensíveis em setores prioritários. pp 1–68.
2. Energy Statistics (2019) https://www.iea.org/reports/world-energy-statistics-2019. accessed 21 Sept 2020.
3. Dutta S (2014) A review on production, storage of hydrogen and its utilization as an energy resource. J Ind Eng Chem 20:1148–1156
4. da Silva Veras T, Mozer TS, da Silva César A (2017) Hydrogen: trends, production and characterization of the main process worldwide. Int J Hydrogen Energy 42:2018–2033
5. Demirbas A (2017) Future hydrogen economy and policy. Energy Sources B Econ Plan Policy 12:172–181
6. Moravvej Z, Soroush E, Makarem MA, Rahimpour MR (2021) 7. Thermochemical routes for hydrogen production from biomass. Elsevier, Amsterdam, pp 193–208
7. Ochoa A, Bilbao J, Gayubo AG, Castaño P (2020) Coke formation and deactivation during catalytic reforming of biomass and waste pyrolysis products: a review. Renew Sustain Energy Rev 119:109600
8. Mattos LV, Jacobs G, Davis BH, Noronha FB (2012) Production of hydrogen from ethanol: review of reaction mechanism and catalyst deactivation. Chem Rev 112:4094–4123
9. Sun J, Wang Y (2014) Recent advances in catalytic conversion of ethanol to chemicals. ACS Catal 4:1078–1090
10. Zanchet D, Santos JBO, Damyanova S, Gallo JMR, Bueno JMC (2015) Toward understanding metal-catalyzed ethanol reforming. ACS Catal 5:3841–3863
11. Li S, Gong J (2014) Strategies for improving the performance and stability of Ni-based catalysts for reforming reactions. Chem Soc Rev 43:7245–7256
12. Auprêtre F, Descorme C, Duprez D (2002) Bio-ethanol catalytic steam reforming over supported metal catalysts. Catal Commun 3:263–267
13. Frusteri F, Freni S, Spadaro L, Chiodo V, Bonura G, Donato S, Cavallaro S (2004) H$_2$ production for MC fuel cell by steam reforming of ethanol over MgO supported Pd, Rh, Ni and Co catalysts. Catal Commun 5:611–615
14. de Lima SM, da Silva AM, da Costa LOO, Assaf JM, Jacobs G, Davis BH, Mattos LV, Noronha FB (2010) Evaluation of the performance of Ni/La$_2$O$_3$ catalyst prepared from LaNiO$_3$ perovskite-type oxides for the production of hydrogen through steam reforming and oxidative steam reforming of ethanol. Appl Catal A 377:181–190
15. Chen H, Yu H, Peng F, Yang G, Wang H, Yang J, Tang Y (2010) Autothermal reforming of ethanol for hydrogen production over perovskite LaNiO$_3$. Chem Eng J 160:333–339
16. Liu F, Qu Y, Yue Y, Liu G, Liu Y (2015) Nano bimetallic alloy of Ni–Co obtained from LaCo$_x$Ni$_{1-x}$O$_3$ and its catalytic performance for steam reforming of ethanol. RSC Adv 5:16837–16846
17. Pena MA, Fierro JLG (2001) Chemical structures and performance of perovskite oxides. Chem Rev 101:1981–2018
18. Atta NF, Galal A, Ekram H (2016) Perovskite nanomaterials-synthesis, characterization, and applications. InTech, London
19. Peng Z, Somodi F, Helveg S, Kisielowski C, Specht P, Bell AT (2012) High-resolution in situ and ex situ TEM studies on graphene formation and growth on Pt nanoparticles. J Catal 286:22–29
20. Ribeiro RU, Liberatori JWC, Winnishofer H, Bueno JMC, Zanchet D (2009) Colloidal Co nanoparticles supported on SiO$_2$: synthesis, characterization and catalytic properties for steam reforming of ethanol. Appl Catal B 91:670–678
21. Toniolo FS, Schmal M (2016) Improvement of catalytic performance of perovskites by partial substitution of cations and supporting on high surface area materials. InTech, London
22. Yi N, Cao Y, Su Y, Dai W-L, He H-Y, Fan K-N (2005) Nanocrystalline LaCoO$_3$ perovskite particles confined in SBA-15 silica as a new efficient catalyst for hydrocarbon oxidation. J Catal 230:249–253
23. Zhang J, Weng X, Wu Z, Liu Y, Wang H (2012) Environmental facile synthesis of highly active LaCoO$_3$/MgO composite perovskite via simultaneous co-precipitation in supercritical water. Appl Catal B 126:231–238
24. Wang N, Yu X, Wang Y, Chu W, Liu M (2013) A comparison study on methane dry reforming with carbon dioxide over LaNiO$_3$ perovskite catalysts supported on mesoporous SBA-15, MCM-41 and silica carrier. Catal Today 212:98–107
25. Marinho ALA, Rabelo-Neto RC, Noronha FB, Mattos LV (2016) Steam reforming of ethanol over Ni-based catalysts obtained from LaNiO$_3$ and LaNiO$_3$/CeSiO$_2$ perovskite-type oxides for the production of hydrogen. Appl Catal A 520:53–64
26. Toniolo FS (2010) Óxidos mistos do tipo perovskita para a geração de gás de síntese. UFRJ, Tese Doutorado
27. Zhao D, Feng J, Huo Q, Melosh N, Fredrickson GH, Chmelka BF, Stucky GD (1998) Triblock copolymer syntheses of mesoporous silica with periodic 50 to 300 angstrom pores. Science 279:548–552
28. Zhao D, Huo Q, Feng J, Chmelka BF, Stucky GD (1998) Nonionic triblock and star diblock copolymer and oligomeric surfactant syntheses of highly ordered, hydrothermally stable, mesoporous silica structures. J Am Chem Soc 7863:6024–6036
29. Oemar U, Kathiraser Y, Mo L, Ho XK, Kawi S (2016) CO$_2$ reforming of methane over highly active La-promoted Ni

supported on SBA-15 catalysts: mechanism and kinetic modelling. Catal Sci Technol 6:1173–1186

30. Zhao L, Han T, Wang H, Zhang L, Liu Y (2016) Environmental Ni–Co alloy catalyst from LaNi$_{1-x}$Co$_x$O$_3$ perovskite supported on zirconia for steam reforming of ethanol. Appl Catal B 187:19–29

31. Li S, Tang H, Gong D, Ma Z, Liu Y (2017) Loading Ni/La$_2$O$_3$ on SiO$_2$ for CO methanation from syngas. Catal Today 297:298–307

32. Rivas I, Alvarez J, Pietri E, Pérez-Zurita MJ, Goldwasser MR (2010) Perovskite-type oxides in methane dry reforming: effect of their incorporation into a mesoporous SBA-15 silica-host. Catal Today 149:388–393

33. Xiao P, Zhu J, Li H, Jiang W, Wang T, Zhu Y, Zhao Y, Li J (2014) Effect of textural structure on the catalytic performance of LaCoO$_3$ for CO oxidation. ChemCatChem 6:1774–1781

34. Rabelo-Neto RC, Sales HBE, Inocêncio CVM, Varga E, Oszko A, Erdohelyi A, Noronha FB, Mattos LV (2018) CO$_2$ reforming of methane over supported LaNiO$_3$ perovskite-type oxides. Appl Catal B Environ 221:349–361

35. Albuquerque MCG, Jiménez-Urbistondo I, Santamaría-González J, Mérida-Robles JM, Moreno-Tost R, Rodríguez-Castellón E, Jiménez-López A, Azevedo DCS, Cavalcante CL Jr, Maireles-Torres P (2008) CaO supported on mesoporous silicas as basic catalysts for transesterification reactions. Appl Catal A Gen 334:35–43

36. Grecco STF, Rangel MC, Urquieta-González EA (2013) Zeólitas hierarquicamente estruturadas. Quim Nova 36:131–142

37. Liu J-Y, Su W-N, Rick J, Yang S-C, Pan C-J, Lee J-F, Chen J-M, Hwang B-J (2016) Rational design of ethanol steam reforming catalyst based on analysis of Ni/La$_2$O$_3$ metal–support interactions. Catal Sci Technol 6:3449–3456

38. Li D, Zeng L, Li X, Wang X, Ma H, Assabumrungrat S, Gong J (2015) Environmental ceria-promoted Ni/SBA-15 catalysts for ethanol steam reforming with enhanced activity and resistance to deactivation. Appl Catal B 176–177:532–541

39. Nair MM, Kaliaguine S, Kleitz F (2014) Nanocast LaNiO$_3$ perovskites as precursors for the preparation of coke-resistant dry reforming catalysts. ACS Catal 4:3837–3846

40. Calles JA, Carrero A, Vizcaíno AJ (2009) Ce and La modification of mesoporous Cu–Ni/SBA-15 catalysts for hydrogen production through ethanol steam reforming. Microporous Mesoporous Mater 119:200–207

41. He S, Mei Z, Liu N, Zhang L, Lu J, Li X, Wang J, He D, Luo Y (2017) Ni/SBA-15 catalysts for hydrogen production by ethanol steam reforming: effect of nickel precursor. Int J Hydrogen Energy 42:14429–14438

42. An X, Ren J, Hu W, Wu X, Xie X (2020) A highly efficient and stable Ni/SBA-15 catalyst for hydrogen production by ethanol steam reforming. Prog React Kinet Mech 45:1468678319891842

43. Carrero A, Calles JA, Vizcaíno AJ (2007) Hydrogen production by ethanol steam reforming over Cu–Ni/SBA-15 supported catalysts prepared by direct synthesis and impregnation. Appl Catal A 327:82–94

44. He S, He S, Zhang L, Li X, Wang J, He D, Lu J, Luo Y (2015) Hydrogen production by ethanol steam reforming over Ni/SBA-15 mesoporous catalysts: effect of Au addition. Catal Today 258:162–168

45. Chagas CA, Manfro RL, Toniolo FS (2020) Production of hydrogen by steam reforming of ethanol over Pd-promoted Ni/SiO$_2$ catalyst. Catal Lett 150:3424–3436

46. Zhurka MD, Lemonidou AA, Anderson JA, Kechagiopoulos PN (2018) Kinetic analysis of the steam reforming of ethanol over Ni/SiO$_2$ for the elucidation of metal-dominated reaction pathways. React Chem Eng 3:883–897

47. Arslan A, Gunduz S, Dogu T (2014) Steam reforming of ethanol with zirconia incorporated mesoporous silicate supported catalysts. Int J Hydrogen Energy 39:18264–18272